www.sciencemag.org/cgi/content/full/335/6073/1212/DC1

Supporting Online Material for

An Impactor Origin for Lunar Magnetic Anomalies

Mark A. Wieczorek,* Benjamin P. Weiss, Sarah T. Stewart

*To whom correspondence should be addressed. E-mail: wieczor@ipgp.fr

Published 9 March 2012, *Science* **335**, 1212 (2012)
DOI: 10.1126/science.1214773

This PDF file includes:

SOM Text
Figs. S1 to S8
Tables S1 to S4
References

1 Thermoremanence susceptibility of lunar and meteoritic materials

The thermoremanent magnetization acquired by most rocks is approximately proportional to the magnetizing field for field strengths less than about 50-100 μT (*35–37*). This can be expressed by the relation

$$\mathbf{M}_{tr} = \chi_{TRM}\,\mathbf{H}, \tag{1}$$

where M_{tr} is the thermoremanent magnetization (in units of A m^{-1}), χ_{TRM} is the thermoremanence susceptibility (sometimes denoted by the symbol c (*38*), in SI units), and H is the magnetizing field (in units of A m^{-1}). Experiments show (*39–41*) that the ratio of thermoremnent magnetization to saturation remanent magnetization, M_{rs}, is related linearly to the applied magnetic field B (in units of T)

$$B = a\,M_{tr}/M_{rs}. \tag{2}$$

The proportionality constant a varies by a factor of about 3 to 5 for a wide range of geologic materials, and is about 3×10^{-3} for typical equant grains of multidomain iron (*40*). Using the relation $B = \mu_0 H$, the thermoremanence susceptibility can be expressed as

$$\chi_{TRM} = \mu_0\,M_{rs}/a, \tag{3}$$

where μ_0 is the magnetic constant, $4\pi \times 10^{-7}$ T m A^{-1}.

We gathered measurements of the saturation remnant magnetization per unit mass m_{rs} (in units of A m^2 kg^{-1}; equivalently M_{rs}/ρ, where ρ the sample density) acquired over the last four decades for lunar samples with relatively well-characterized lithologies (Table S1). These include unbrecciated mare basalts, pristine highlands rocks (defined as unbrecciated or monomict anorthosites and Mg-suite rocks uncontaminated by meteoritic materials), and mafic impact melt breccias (as defined by ref. (*22*)). Other highlands breccias (e.g., granulitic breccias) typically are less well-defined petrographically but have similar quantities of ferromagnetic minerals as the mafic impact melt breccias (*5*). The lunar soils and regolith breccias are not considered because the regolith is extremely thin (<15 m (*42*)) and would not

be unidirectionally magnetized given the continuous process of impact gardening. The average magnetic properties of lunar materials are presented in Table S2 under the assumption that the m_{rs} measurements are log-normally distributed. The average magnetic properties of chondritic and achondritic meteorites are given in Table S3.

2 Magnetic field of material magnetized by a central dipole

The Gauss coefficients corresponding to a volume of material magnetized by a now extinct central dipolar field were derived by ref. (*43*). The magnetization in this derivation was confined to lie between an upper surface $r(\theta, \phi)$, where θ and ϕ are respectively colatitude and longitude, and a lower spherical surface with (arbitrary) radius R. The amplitude of the relief r relative to the average value was assumed to be small. The ratio between the acquired thermoremanent magnetization $\mathbf{M}$ and magnetizing field $\mathbf{H}$ was assumed to be linear and equal to χ_{TRM}, and the magnetizing dipolar field was assumed to be aligned with the z axis with a dipole moment p.

Using complex orthonormalized spherical harmonics, Y_l^m, that employ the Condon-Shortley phase of $(-1)^m$ (*44*), the radius of the upper surface was expanded as

$$r(\theta, \phi) = \sum_{l=0}^{L} \sum_{m=-l}^{l} r_l^m \, Y_l^m(\theta, \phi), \tag{4}$$

where l is the spherical harmonic degree, m is the spherical harmonic order, and L is the maximum degree of the expansion. We note that a typographic error is present in their derivation as the average radius of r (here defined to be a) was set equal to r_0^0 instead of $r_0^0/\sqrt{4\pi}$, which is required for the employed spherical harmonic normalization. Nevertheless, ref. (*43*) arrived at the correct results in their discussion, despite this inconsistency. (It is only necessary to replace r_{00} in their manuscript by the average radius of the function r.) The correct equation for the Gauss coefficients, after taking into

account an additional selection rule not used by ref. (*43*), is

$$
\begin{aligned}
g_l^m &= \frac{c\,p\,\mu_0}{4\,\pi\,a^3} \sum_{l'=l-1,l+1} \frac{r_{l'}^m}{a} \sqrt{\frac{2l'+1}{(2l+1)^3}}\, C_{10l'0}^{l0} \\
&\quad \times \left[(2l-2-m)\, C_{10l'm}^{lm} - \sqrt{2} \sqrt{l'(l'+1) - m(m+1)}\, C_{1,-1,l',m+1}^{lm} \right],
\end{aligned}
\tag{5}
$$

where the sum over l' is understood to be only for the two listed values. The relation between Schmidt semi-normalized, g_{lm}, and the above complex normalized coefficients is

$$
g_{lm} = \sqrt{\frac{2l+1}{4\pi}} \begin{cases} g_l^0 & m = 0 \\ (-1)^m\ \sqrt{2}\ \text{Real}\,(g_l^m) & m > 0 \\ (-1)^{m+1}\ \sqrt{2}\ \text{Imag}\left(g_l^{|m|}\right) & m < 0. \end{cases}
\tag{6}
$$

The magnetic potential is given by the expression

$$
U(\mathbf{r}) = a \sum_{l=1}^{L} \sum_{m=-l}^{l} \left(\frac{a}{r}\right)^{l+1} g_{lm}\, Y_{lm}(\theta, \phi),
\tag{7}
$$

where the spherical harmonic functions Y_{lm} are Schmidt semi-normalized, and the magnetic field $\mathbf{B}$ is equal to the gradient of the potential

$$
\mathbf{B}(\mathbf{r}) = -\nabla U(\mathbf{r}).
\tag{8}
$$

For computational purposes, we note that the Wigner 3-j symbols are related to the Clebsch-Gordan coefficients by (*44, p. 236*)

$$
C_{l_1 m_1 l_2 m_2}^{lm} = (-1)^{l_1 - l_2 + m} \sqrt{2l+1} \begin{pmatrix} l_1 & l_2 & l \\ m_1 & m_2 & -m \end{pmatrix}.
\tag{9}
$$

3 Impact simulation methods

The formation of impact basins approximately the size of South Pole-Aitken was modeled using the CTH shock physics code (*45*) in three dimensions with self-gravity (*46*). The Moon was initialized in gravitational equilibrium with an estimate for the 0.5 Gyr thermal profile (*47*), and given the early time of the South Pole-Aitken impact, molten cores were assumed for both the projectile and Moon. Multiphase model equations of state were used for molten iron (*48*), forsterite (2008 update by Melosh based on

ref. (*49*)), and silica (*50*) to represent core, mantle, and crustal materials, respectively. The simulations utilized the adaptive mesh refinement feature in CTH. Since the simulations were performed in Cartesian geometry, for visualization purposes, the thickness of crustal and projectile materials were determined by projecting and summing the mass of these materials onto an approximately 130 km by 130 km equal area grid at the surface.

The projectile had a resolution of 5 or 10 km until the shock wave was fully released. The crust and upper mantle resolution was typically 20 km in the impacted hemisphere, and sensitivity tests were run with resolutions of 10 to 40 km. Though these resolutions were sufficient to quantify the size of the region were the crust was entirely excavated and the general redistribution of the crust, these resolutions (in combination with the coarse grid used for visualization) are probably too low to quantify the fine details of the post-impact stratigraphy. The overall distribution and thickness of proximal ejecta materials, which is the main purpose of this study, was found to be qualitatively similar in these resolution tests, with differences of a factor of about three (Figs. S1 and S5). It is emphasized that this factor of three is small in comparison to the uncertainty in the strength of the field that magnetized these deposits, which is estimated to be between about 1 to 120 μT (*5, 20*). In Figs. S1-S8, the mottled appearance of the crustal thickness on the opposite hemisphere of the impact basin is an artifact due to a lower resolution of the crust in this region. Vaporized and finely dispersed materials are removed from the calculation for computational expediency using a density criteria (typically 0.1 kg m^{-3}).

The pressure, temperature, and strain-rate dependent rheological model was an updated version of ref. (*28*). In this work, the dynamic weakening criteria includes the effect of overburden pressure (*51,52*). The lunar crust was modeled with the parameters for granite in ref. (*28*). For the mantle, the limiting yield surface was defined by dislocation creep for olivine based on laboratory experiments (*53*). The peridotite solidus and olivine liquidus were used to calculate melting in the mantle (*54*), which was implemented in a similar manner as in ref. (*55*). Iron was assumed to be hydrodynamic.

The sizes of the excavation cavity and the final basin diameter were not significantly affected by these

updates to the rheological model used in ref. (*28*). One change affects our investigation of the distribution of materials near the basin rim. In previous numerical simulations of impact cratering, materials heated to and above the solidus were essentially modeled as hydrodynamic fluids. It has long been recognized that the depth of shock-induced melting exceeds the excavation depth in basin-forming events (*56*). Thus, in such large impacts, the collapse of the transient cavity involves significant amounts of melted material. As a result, the gravitationally-driven collapse of the transient crater led to overshoot and sloshing of mantle materials onto the surrounding crust (*55*); however, widespread surface deposits of mantle materials are not observed around South Pole-Aitken basin.

In this work, it is recognized that the collapse of the mantle involves a two-phase flow of melt and solid clasts. Under the high strain rates of crater collapse, the ratio of clast inertia to viscous forces (the Bagnold number) is high; as a result, the shear stresses are determined by collisions between the solid clasts (*57*). Furthermore, the convergent geometry ensures a high volume fraction of clasts mixing into the melt. Here, this complex debris flow of mantle materials was modeled using a simplified approach: when the temperature exceeded the solidus, a pressure-dependent friction law (coefficient of 0.1 to 0.2 based on melt-lubricated faults (*58*)) was used at high strain rates ($>10^{-4}$ s^{-1}), and a Newtonian fluid rheology was used at low strain rates when the viscosity of the fluid dominates (*59*).

During collapse of the transient cavity, the frictional strength of the melt-clast mixture inhibits significant overshoot of mantle material. As a result, most of the deposits near the basin rim are primary ejecta from the excavation cavity. In the three-dimensional simulations, the basin structure about an hour after the impact has two major features: (i) an inner region filled with a mixture of melt and solid clasts and bounded by the cold crust folded over at the rim of the excavation cavity, and (ii) a terrace of thinned and translated cold crust surrounded by the original crust thickened by ejecta deposits. We identify the boundary between the thinned terrace and thickened crust as the approximate final basin diameter, which is analogous to the outer ellipse in Fig. 1. The thickest crust in our simulations is located in the downrange direction, consistent with the thickened crust north of the South Pole-Aitken basin as derived from

gravity and topography data (*11*) (though see (*60*) for a non-impact explanation for this thickened crust).

Most of the crust in the inner region, denoted by white lines in Figs. 3 and S1 to S8, was excavated during formation of the transient cavity; some crustal materials remain trapped beneath the projectile and are melted and partially vaporized by the impact shock. The deep thermal anomaly from the impact has a diameter slightly larger than the region of excavated crust. We hypothesize that this melt pool fractionally crystallizes (*61*), possibly incorporating portions of the adjacent crust, to form a new, thinner crust in the inner basin. This secondary crust would correspond to the mafic geochemical anomaly associated with the interior of the South Pole-Aitken basin, approximated by the inner solid white line in Fig. 1. In all cases studied here, the basin is approximately circular. However, the hot inner region is offset downrange from center, and post-impact modification may affect the final shape. In addition, the calculated distributions of crust and projectile materials in and near the hot inner region is likely to be modified during post-impact processes.

We considered impact velocities from 5 to 30 km s^{-1}, impact angles of 30, 45 and 60 degrees, bolide radii from 75 to 260 km, and homogeneous bolides and differentiated bolides with 1/3 core mass fraction. The probability distribution of impact parameters is centered around 45° and 15 km s^{-1} (*62*), where a differentiated projectile 200 km in diameter forms an approximately 2000 km diameter basin. The peak shock pressures were about 120, 250, and 1000 GPa for impact velocities of 10, 15, and 30 km s^{-1}, respectively. The 30 km s^{-1} events led to significant amounts of vaporization of the silicates in the projectile (*63*) and the ejecta deposits lack significant concentrations of the silicate component of the projectile. Much of the vapor escapes the Moon's gravity or is finely dispersed over the lunar surface. Below about 10 km s^{-1}, vaporization is negligible. For the distribution of probable impact velocities, iron in the projectile core undergoes minor amounts of shock-induced vaporization. In 60° events, most of the iron core in differentiated projectiles is jetted from the growing transient cavity at velocities exceeding the escape velocity of the Moon. The amounts of projectile mantle and core retained on the surface of the Moon for all our simulations (excluding the vaporized component that was discarded) are summarized

in Table S4.

During the impact event, the projectile deformed and lined the transient cavity floor, and the vaporized mass fraction escaped on non-ballistic trajectories. The melted and solid portions of the projectile mixed with the lunar crust at the bottom of the transient cavity, and the multi-material code advected the mixed materials together through the mesh. The ballistic ejecta is composed primarily of excavated lunar crust. Figs. S1-S8 present the crustal thickness and integrated thickness of projectile materials mixed into the crust for a selection of simulation runs. The transient cavity formation time was about 500 s, and the basin formation time (including deposition of the continuous ejecta blanket) was about 1 hour. The simulations were run typically for more than one hour, with some cases up to 4 hours to examine far-field ejecta. Some of the high velocity ejecta passed beyond the spatial confines of the simulation domain and were removed from consideration. The deposition of ejecta on the opposite hemisphere of the Moon would be affected by the Moon's rotation (*64*), which is not accounted for in our simulations.

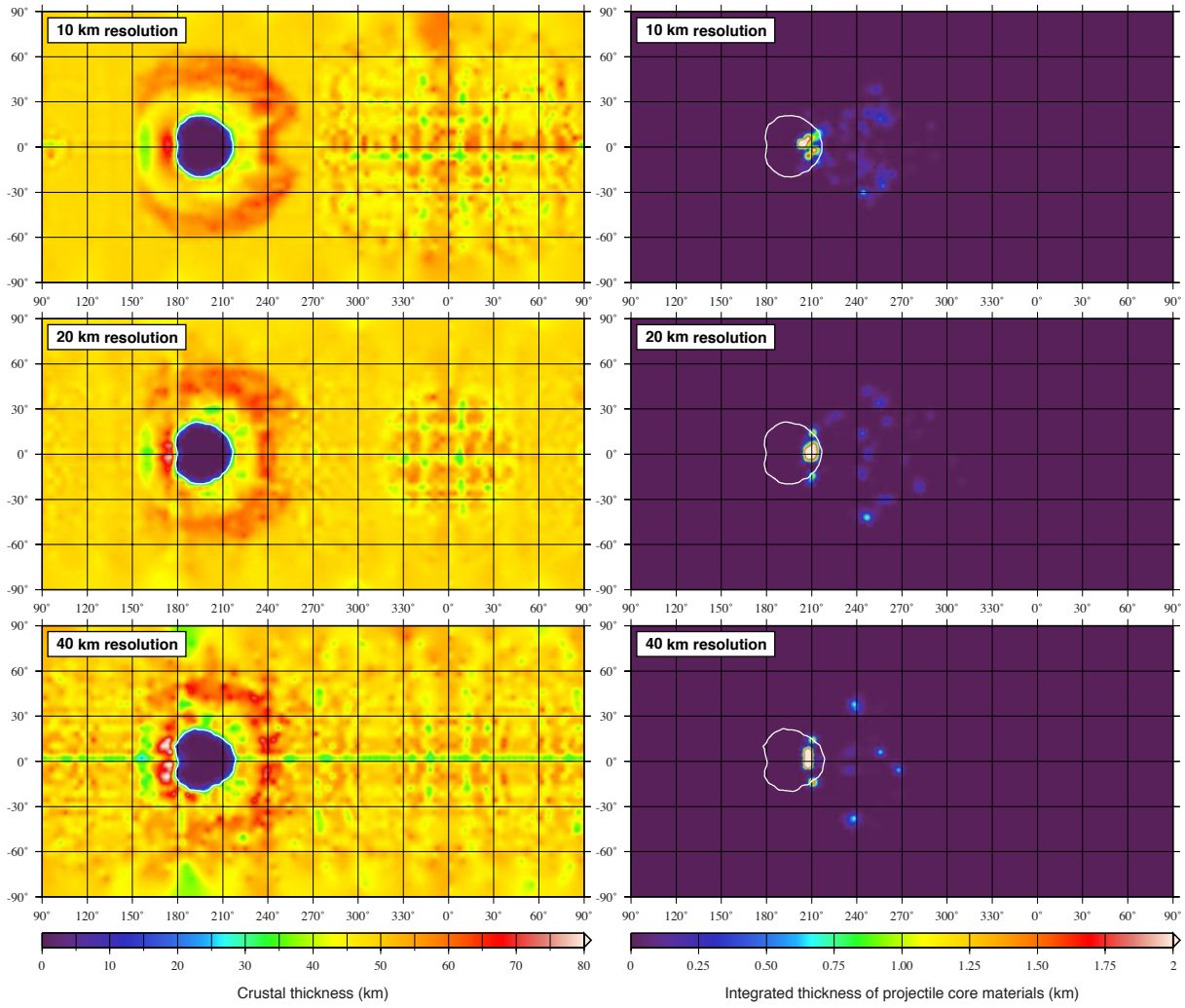

Fig. S1. Comparison of simulation results with different spatial resolutions of the lunar crust. Crustal thickness (left) and integrated thickness of projectile core materials (right) are shown for simulations with 10-km (top), 20-km (middle), and 40-km (bottom) resolutions in the crust of the impacted hemisphere. For these oblique impact simulations, the impact direction was from left to right, the impact velocity was 15 km s^{-1}, the impact angle from vertical was 45°, and the projectile was differentiated with a 100 km radius and a 55 km radius core. The map projection is simple cylindrical, and the solid white contour denotes where the crustal thickness has been reduced by a factor of two. The maximum integrated thickness of core materials is 5.4, 4.1, and 5.6 km for the 10, 20, and 40 km resolution simulations, respectively. Results for these tests are shown 55 minutes following the impact.

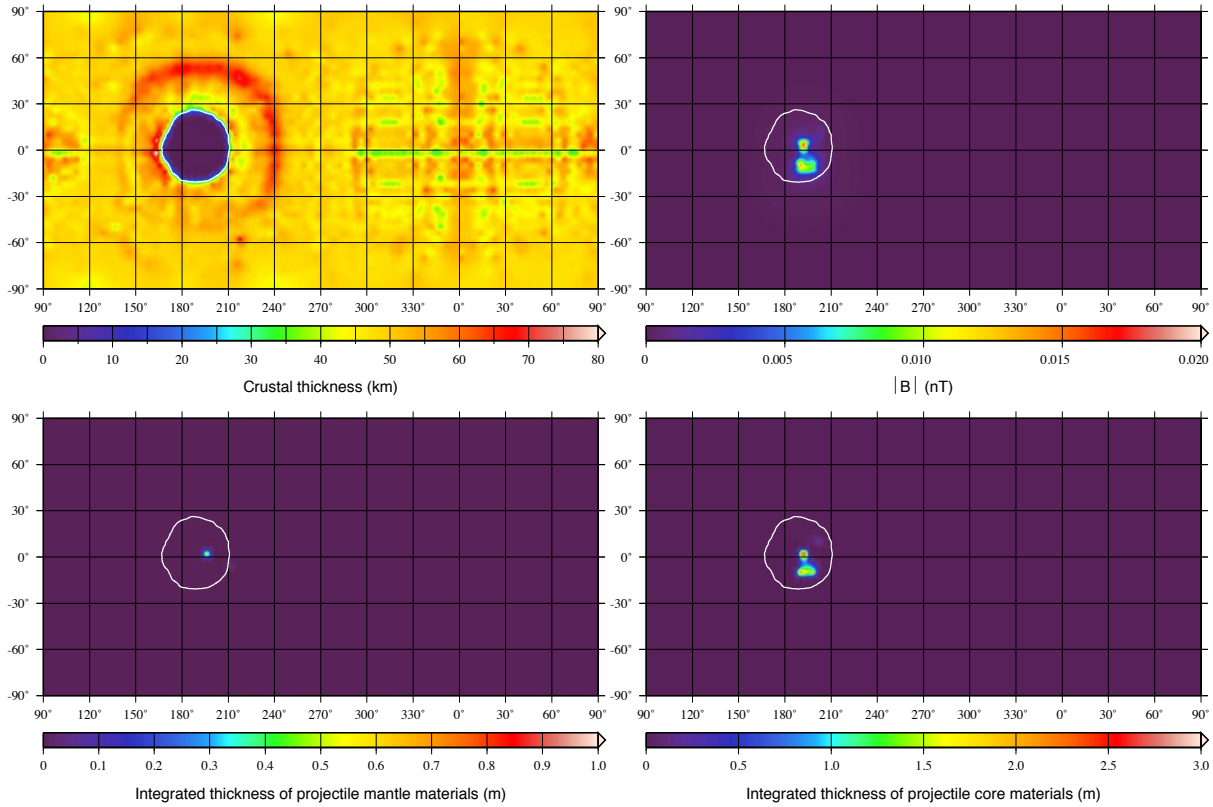

Fig. S2A. Crustal thickness (top left), integrated projectile mantle thickness (bottom left), integrated projectile core thickness (bottom right), and predicted magnetic field strength (top right) for a representative South Pole-Aitken basin forming impact event. For this oblique impact simulation, the impact direction was from left to right, the impact velocity was 30 km s^{-1}, the impact angle from vertical was 30°, and the 75 km radius projectile was differentiated with a 41 km radius core. The projectile mantle component delivered to the Moon was assumed to possess the thermoremanence susceptibility of eucrite meteorites (6.59×10^{-4} SI units), whereas the projectile core materials were assumed to possess a thermoremanence susceptibility of 0.5 SI units, which is representative of ordinary and enstatite chondrites. The magnetic field strength was determined by assuming the projectile materials acquired a thermoremanent magnetization in a dipolar field with a surface field strength of 5 μT. The map projection is simple cylindrical, and the solid white contour denotes where the crustal thickness has been reduced by a factor of two. The simulations had a resolution in the crust of 20 km on the impacted hemisphere, and the results are shown 67 minutes following the impact.

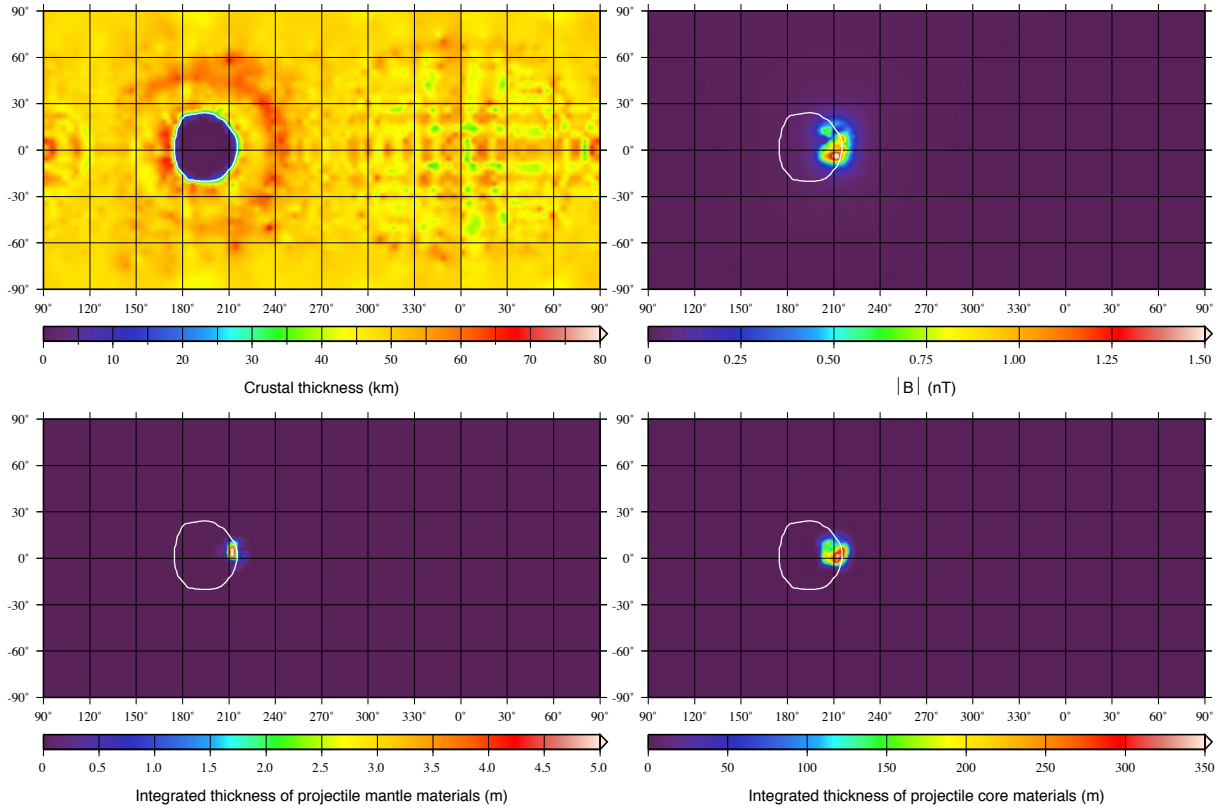

Fig. S2B. Same as Fig. S2A, but for an impact angle of 45° from vertical.

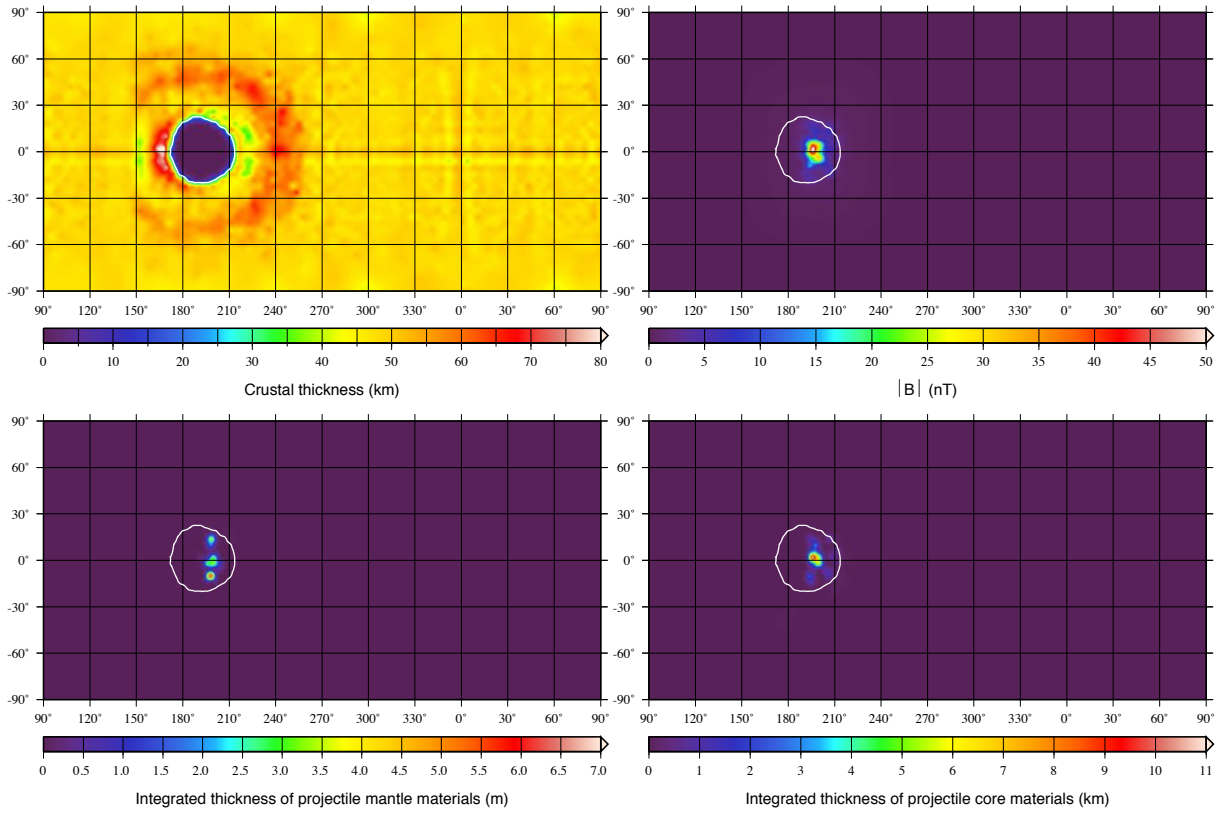

Fig. S3A. Impact of a 100 radius differentiated projectile with a 55 km radius core, an impact velocity of 15 km s^{-1}, and an impact angle of 30° from vertical. Format and other parameters the same as in Fig. S2A.

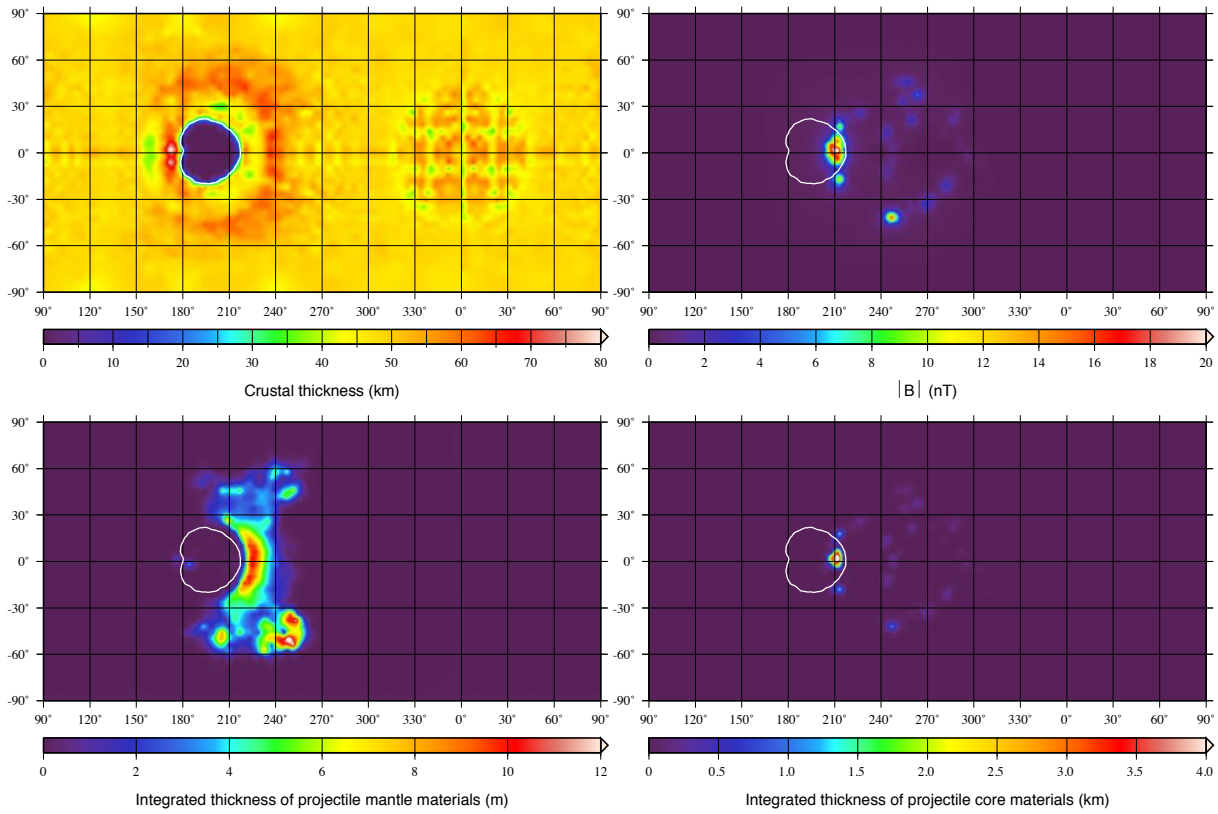

Fig. S3B. Same as Fig. S3A, but for an impact angle of 45° from vertical.

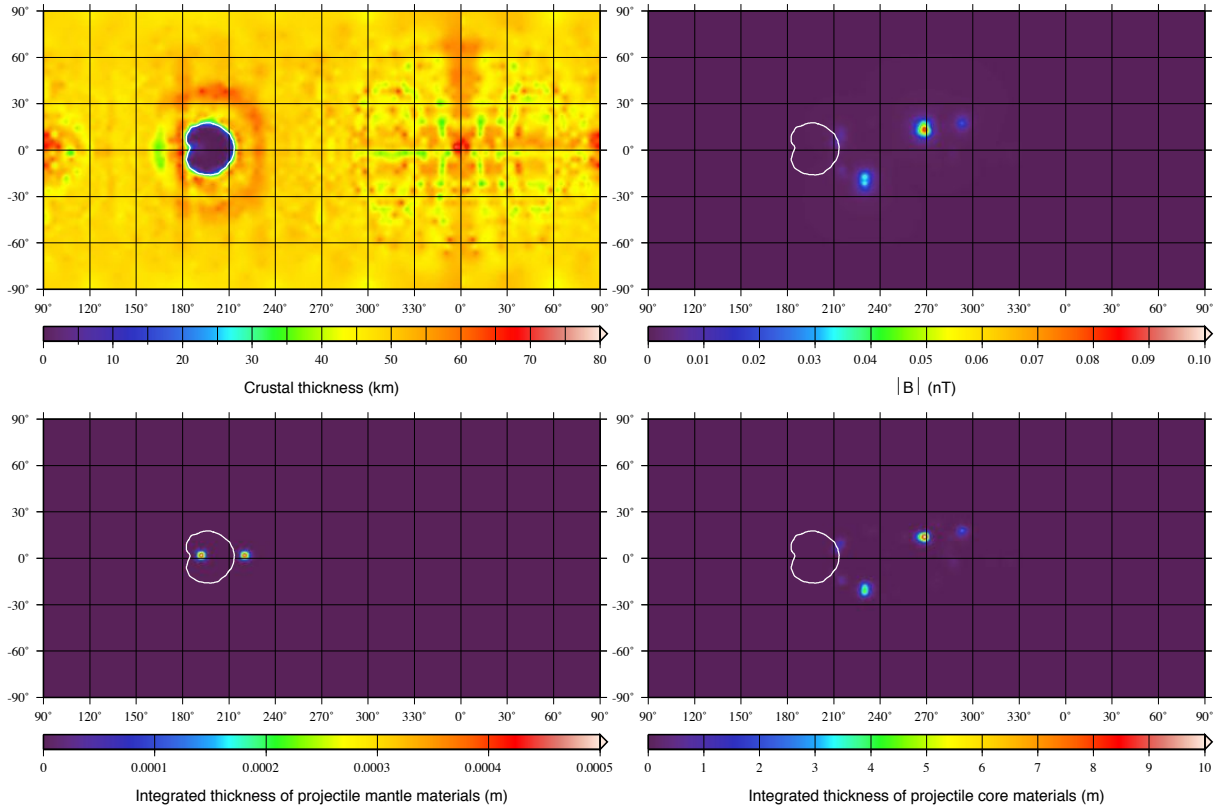

Fig. S3C. Same as Fig. S3A, but for an impact angle of 60° from vertical.

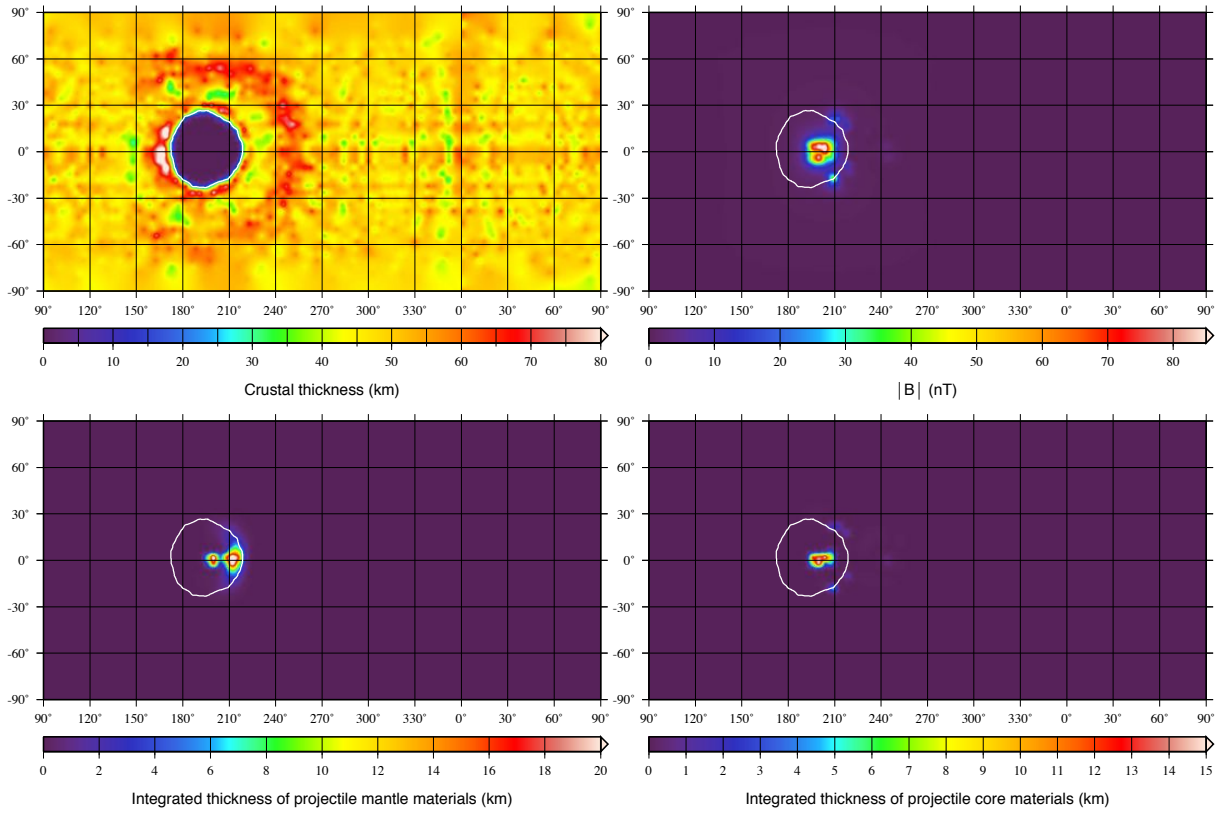

Fig. S4A. Impact of a 130 km radius differentiated projectile with a 71 km radius core, an impact velocity of 10 km s^{-1}, an impact angle of 30° from vertical, and a simulation resolution in the crust of 40 km. Format and other parameters the same as in Fig. S2A.

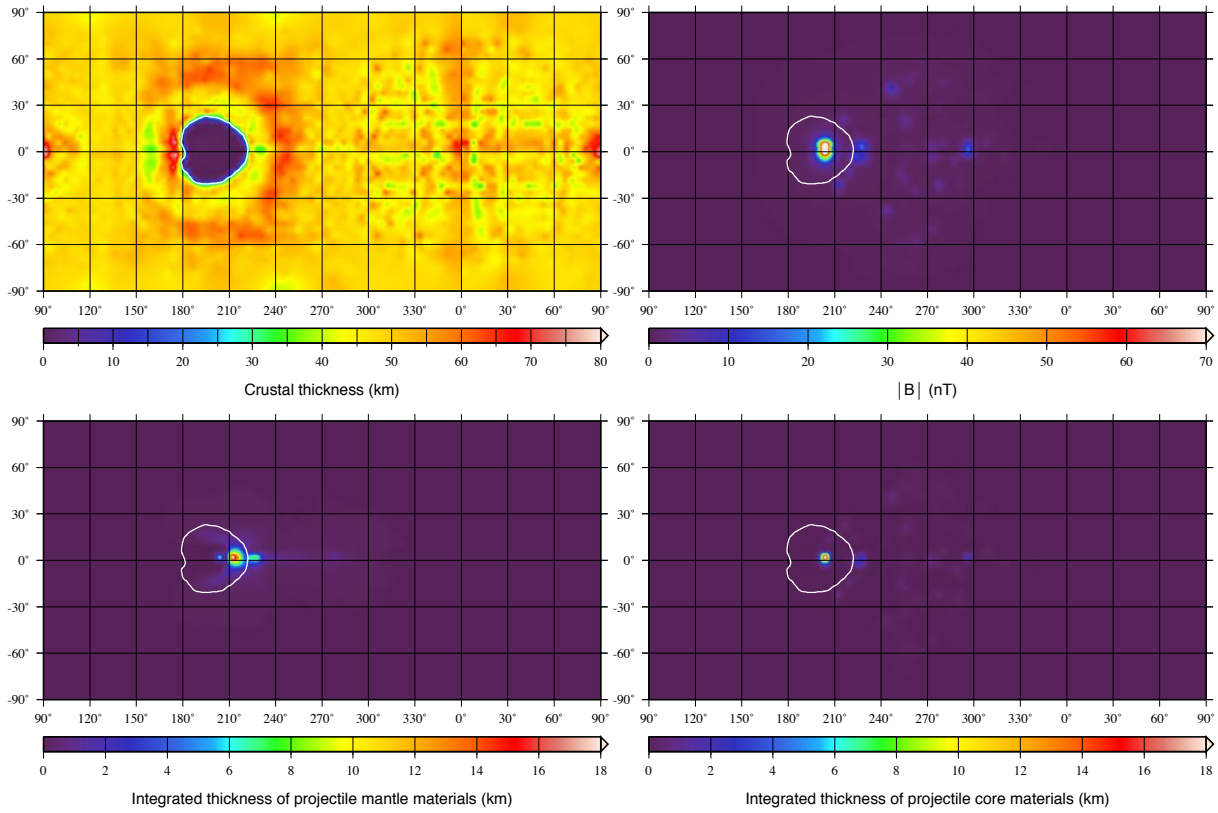

Fig. S4B. Same as Fig. S4A, but for an impact angle of 45° from vertical, and a simulation resolution in the crust of 20 km.

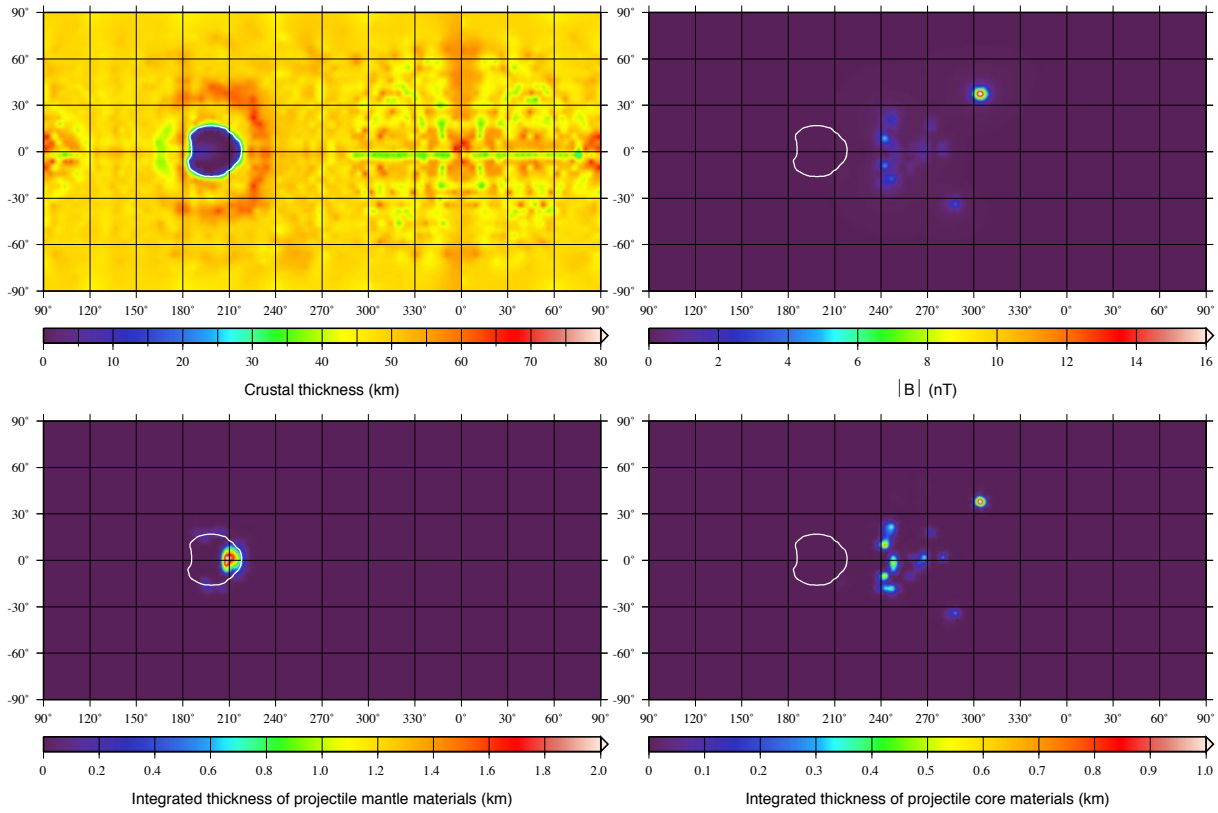

Fig. S4C. Same as Fig. S4A, but for an impact angle of 60° from vertical, and a simulation resolution in the crust of 20 km.

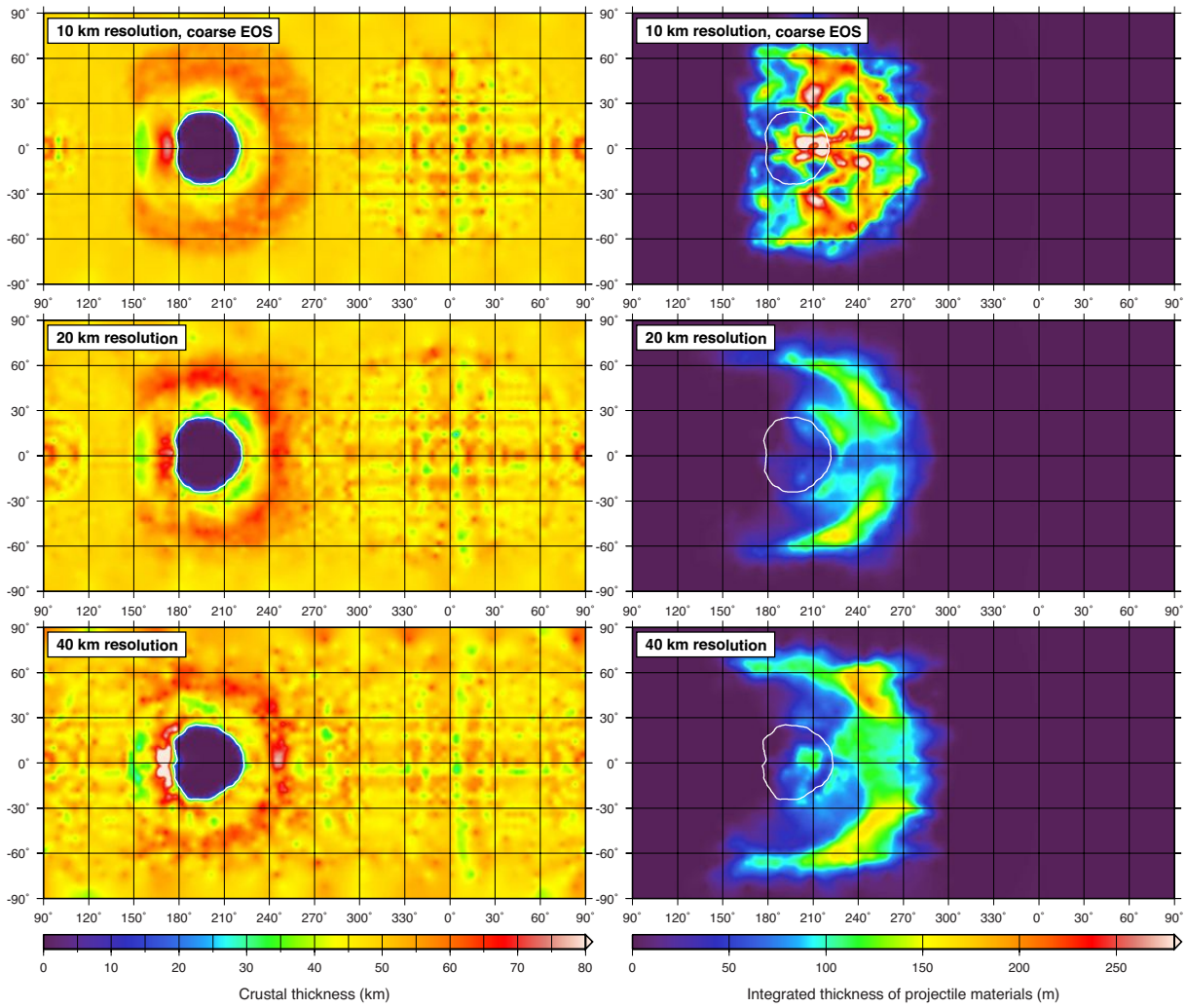

Fig. S5. Comparison of simulation results with different resolutions of the lunar crust and different resolution tabulations of the equation of state. Crustal thickness (left) and integrated thickness of projectile materials (right) are shown for simulations with 10-km (top), 20-km (middle), and 40-km (bottom) resolutions in the crust on the impacted hemisphere. For these oblique impact simulations, the impact direction was from left to right, the impact velocity was 15 km s^{-1}, the impact angle from vertical was 45°, and the projectile was homogeneous in material properties with a 125 km radius. The map projection is simple cylindrical, and the solid white contour denotes where the crustal thickness has been reduced by a factor of two. The 10-km case used a more coarsely gridded equation of state table than the other two simulations. The maximum integrated thicknesses of projectile materials are 437, 171, and 217 km, which are shown 66 minutes following the impact, for the 10, 20, and 40 km resolution simulations, respectively.

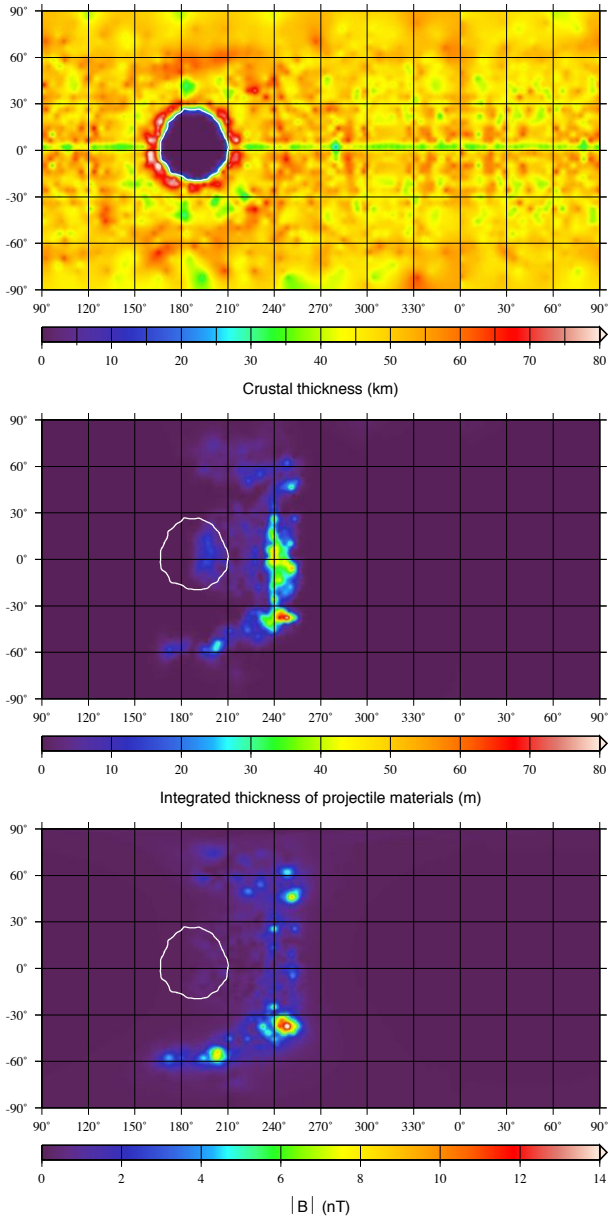

Fig. S6A. Crustal thickness (top), integrated projectile thickness (middle), and predicted magnetic field strength (bottom) for a representative South Pole-Aitken basin forming impact event. For this oblique impact simulation, the impact direction was from left to right, the impact velocity was 30 km s^{-1}, the impact angle from vertical was 30°, and the projectile was homogeneous with a 79 km radius. The simulation resolution in the crust was 40 km. The projectile component delivered to the Moon was assumed to possess the average thermoremanence susceptibility of chondritic meteorites (0.453 SI units), and the magnetic field strength was determined by assuming the projectile materials acquired a thermoremanent magnetization in a dipolar field with a surface field strength of 100 μT. The map projection is simple cylindrical, and the solid white contour denotes where the crustal thickness has been reduced by a factor of two. The simulation results are shown 83 minutes following the impact.

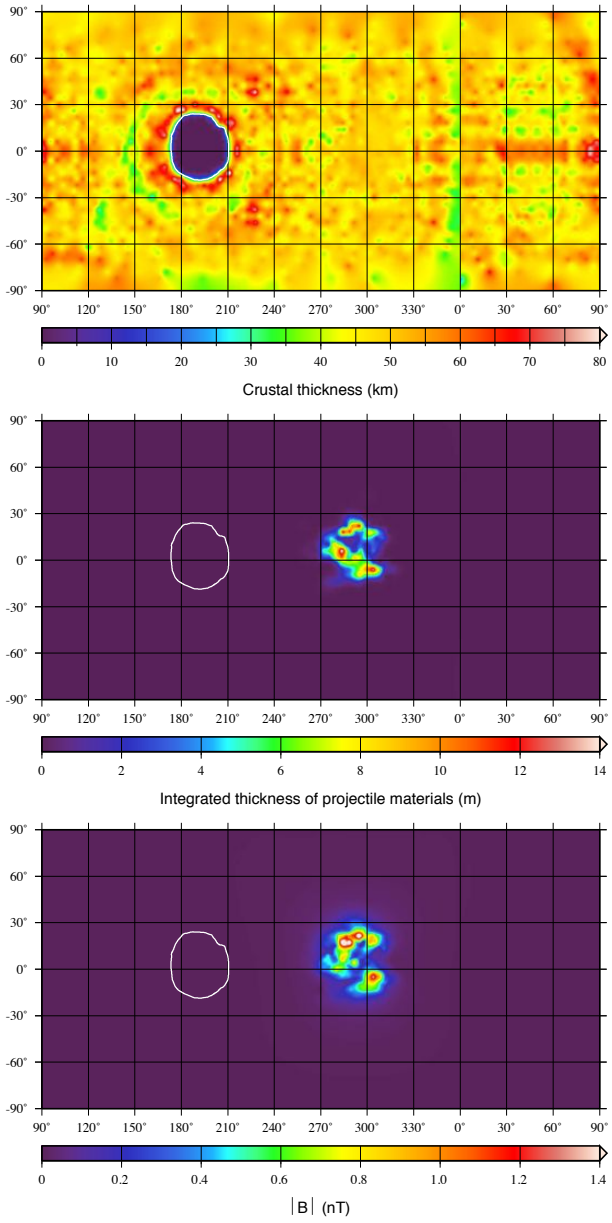

Fig. S6B. Same as Fig. S6B, but for an impact angle of 45° from vertical, and 2.8 hours following the impact.

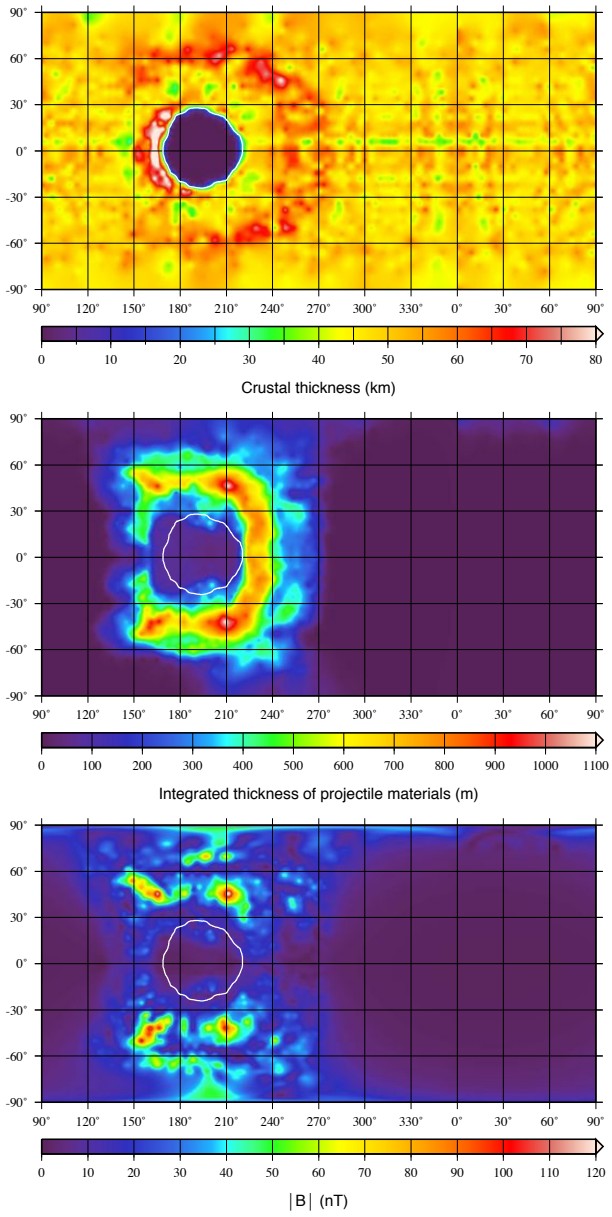

Fig. S7A. Impact of a 125 km radius homogeneous projectile at an impact velocity of 15 km s^{-1} and an impact angle of 30° from vertical. Results are shown 67 minutes following the impact. Format and other parameters the same as in Fig. S6A.

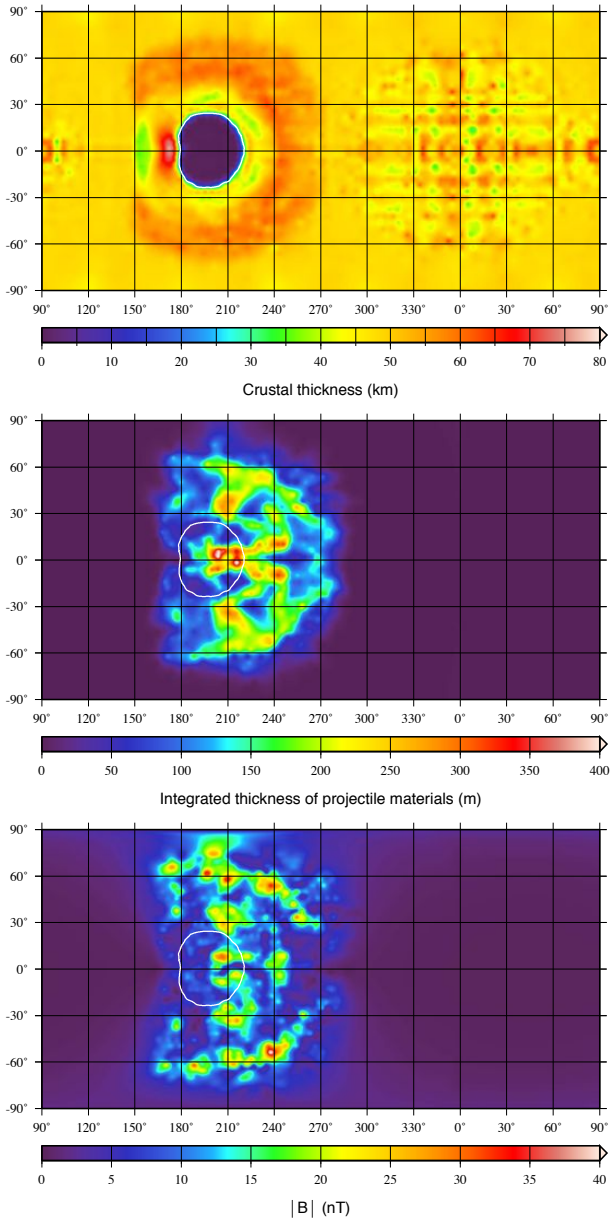

Fig. S7B. Same as Fig. S7A, but for an impact angle of 45° from vertical, a simulation resolution in the crust of 10 km, and 67 minutes following the impact.

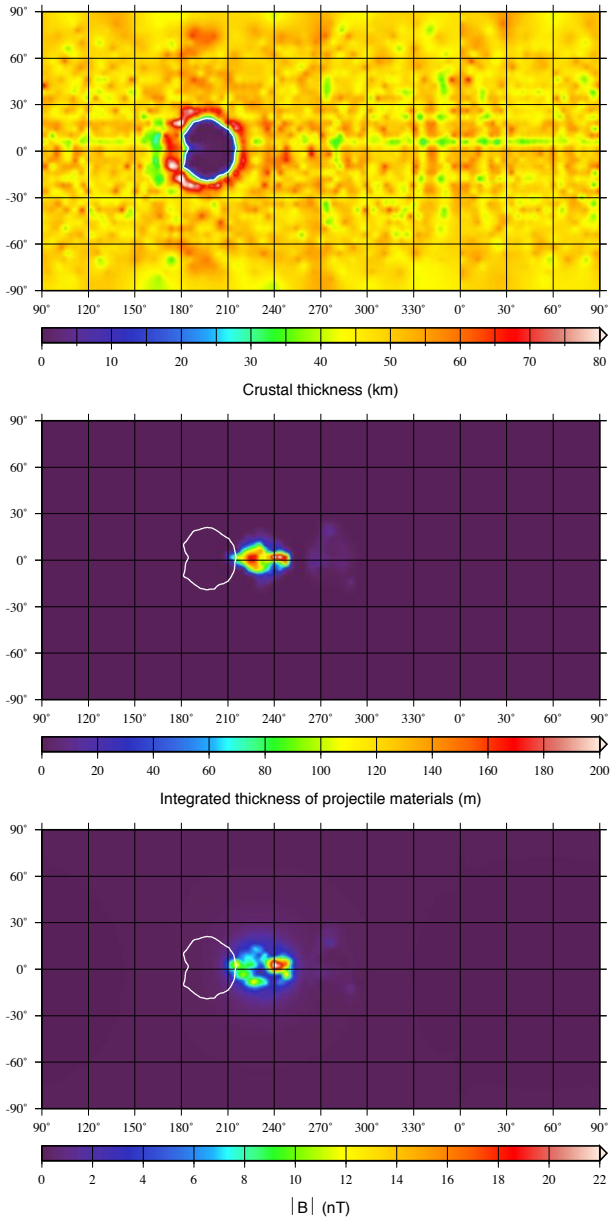

Fig. S7C. Same as Fig. S7A, but for an impact angle of 60° from vertical, and 67 minutes following the impact.

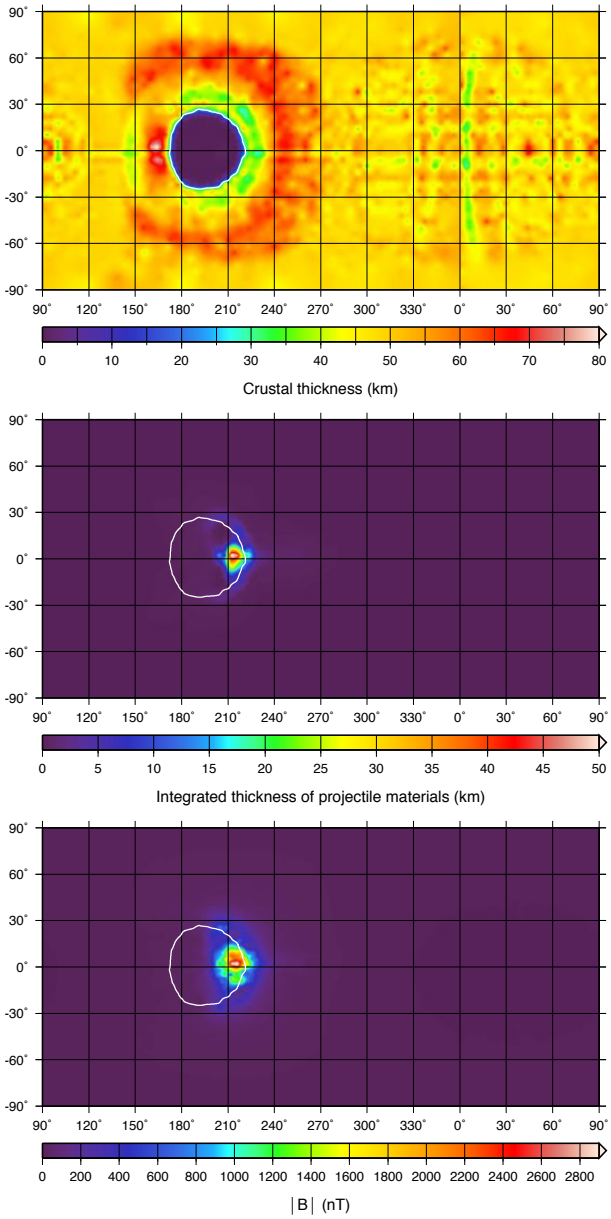

Fig. S8A. Impact of a 150 km radius homogeneous projectile at an impact velocity of 10 km s^{-1} and an impact angle of 30° from vertical. Results are shown 65 minutes following the impact, and the crustal resolution is 20 km. Format and other parameters the same as in Fig. S6A.

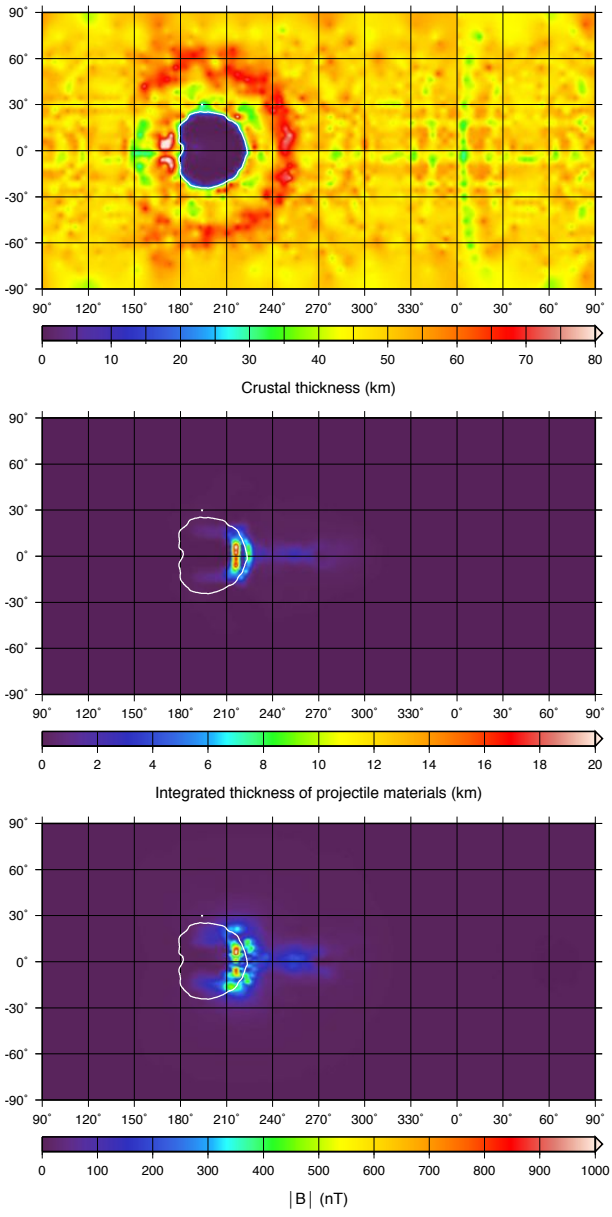

Fig. S8B. Same as Fig. SBA, but for an impact angle of 45° from vertical, a simulation resolution in the crust of 10 km, and 67 minutes following the impact.

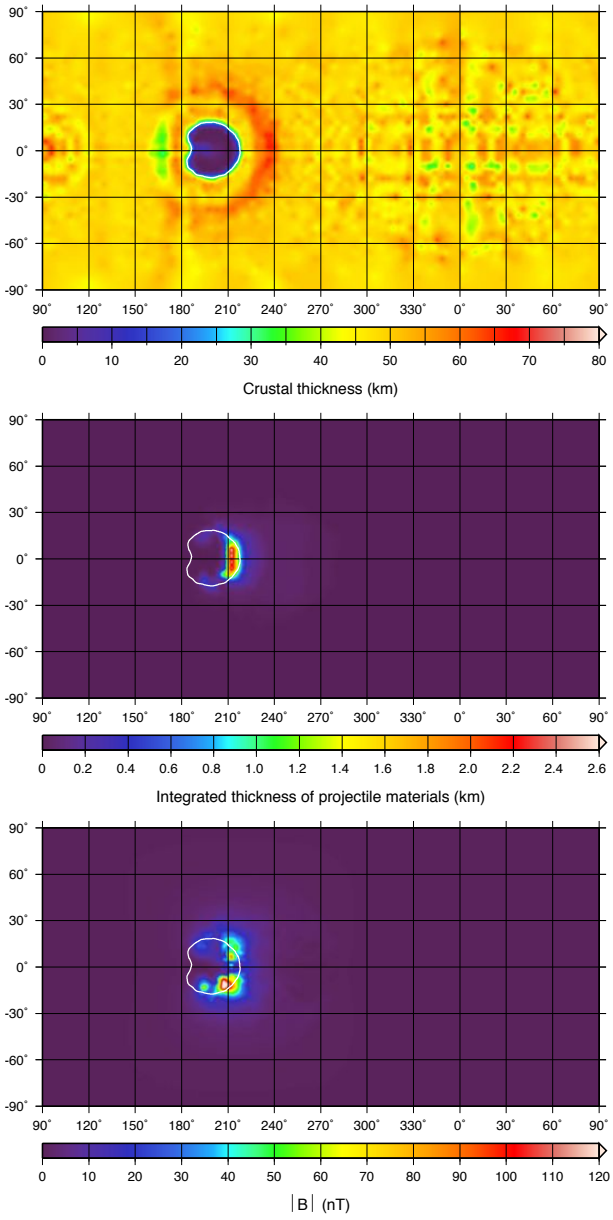

Fig. S8C. Same as Fig. S8A, but for an impact angle of 60° from vertical, and 67 minutes following the impact.

Table S1. Saturation remanent magnetization per unit mass m_{rs} of lunar rocks in A m^2 kg^{-1}.

Sample number	$\log_{10} m_{rs}$	Source
Mare basalts		
10003	-3.347	(*65*)
10017	-3.108	(*65*)
10020	-2.921	(*65*)
	-3.125	(*66*)
10024	-2.824	(*67,68*)
10047	-3.602	(*65*)
	-3.658	(*69*)
10049	-2.831	(*70*)
10050	-3.137	(*65*)
10057	-2.854	(*65*)
10058	-3.699	(*69*)
10062	-3.222	(*69*)
10069	-1.658	(*65*)
12009	-3.190	(*70*)
12022	-3.357	(*70*)
12053	-3.092	(*67,68,71*)
	-3.602	(*69*)
12063	-3.495	(*69*)
12065	-3.523	(*69*)
	-3.056	(*72*)
15016	-3.155	(*72*)
	-3.367	(*65*)
15058	-3.000	(*68,73*)
15076	-2.076	(*72*)
15495	-3.125	(*73*)
15499	-3.090	(*70*)
	-3.000	(*65*)
15555	-3.000	(*73*)
	-3.456	(*72*)
15556	-2.824	(*73*)
	-2.886	(*73*)
15595	-3.108	(*72*)
15597	-3.342	(*70*)
	-3.409	(*65*)
70017	-2.045	(*74*)
	-3.000	(*75*)
	-2.824	(*75*)
70035	-2.592	(*76*)
	-2.770	(*65*)
70135	-2.745	(*65*)

Sample number	$\log_{10} m_{rs}$	Source
70215	-2.770	(*76*)
	-2.357	(*75*)
71055	-2.071	(*74*)
75055	-3.333	(*76*)
74275	-2.260	(*76*)
	-2.112	(*74*)
78505	-2.721	(*65*)
79155	-2.387	(*65*)
NWA 032	-2.852	(*19*)
NWA 4734	-2.150	(*19*)
Mg-suite norites		
78235	-2.487	This study, (*77*)
Mg-suite troctolites		
76535	-3.220	(*20*)
Pristine anorthosites		
60015	-4.137	(*65*)
60025	-5.301	(*65*)
Mafic impact melt breccias		
60315	-3.155	(*73*)
	-3.071	(*78*)
61156	-2.523	(*75*)
	-2.222	(*75*)
14303	-1.678	(*68*)
14311	-2.367	(*68*)
14312	-2.268	(*5*)
14321	-2.108	(*5*)
66095	-2.107	(*72*)
	-2.201	(*73*)
15455	-2.678	(*65*)
62235	-1.724	(*79*)
	-2.180	(*65*)
65015	-2.602	(*65*)
77135	-3.086	(*65*)
14305	-2.553	(*65*)

Table S2. Summary of magnetic properties of common lunar rocks: sample type, assumed density ρ, saturation remanent magnetization per unit volume M_{rs}, thermoremanence susceptibility χ_{TRM}, and number of samples N.

Sample type	ρ kg m^{-3}	$M_{rs}^{\dagger}$ A m^{-1}	$\chi_{TRM}^{\dagger}$ SI	N
Mafic impact-melt breccias	3000	$11.7\,(+20.8, -7.5)$	$4.92\,(+8.70, -3.14) \times 10^{-3}$	16
Granulitic breccias	2800	$7.02\,(+8.00, -3.74)$	$2.94\,(+3.35, -1.57) \times 10^{-3}$	5
Pristine Mg-suite rocks	3000	$4.20\,(9.77, 1.81)$	$1.76\,(4.09, 0.76) \times 10^{-3}$	2
Mare basalts	3300	$3.77\,(+7.49, -2.51)$	$1.58\,(+3.14, -1.05) \times 10^{-3}$	50
Pristine feldpathic highland rocks	2800	$5.35\,(20.4, 1.40) \times 10^{-2}$	$2.24\,(8.56, 0.59) \times 10^{-5}$	2

† Multisample averages and ± 1-σ variability in parentheses calculated assuming a log-normal distribution. When only two samples are available, the values in parenthesis correspond to the minimum and maximum values.

Table S3. Magnetic properties of chondritic and achondritic meteorites: meteorite type, assumed density ρ, saturation remanent magnetization per unit volume M_{rs}, and thermoremanence susceptibility χ_{TRM}.

Meteorite Class	$\rho^{\star}$ kg m^{-3}	$M_{rs}^{\dagger}$ A m^{-1}	$\chi_{TRM}^{\dagger}$ SI	Source
Chondrites				
H	3420	$1160\,(+950, -520)$	$0.485\,(+0.398, -0.219)$	(*80*)
L	3360	$443\,(+805, -286)$	$0.186\,(+0.337, -0.120)$	(*80*)
LL	3220	$950\,(+1277, -545)$	$0.398\,(+0.535, -0.228)$	(*80*)
C(2,4,5)	3530	$401\,(+2767, -350)$	$0.168\,(+1.159, -0.147)$	(*81*)
CI	1600	$1060\,(+30, -30)$	$0.443\,(+0.015, 0.014)$	(*81*)
CK4	2850	$3590\,(+840, -680)$	$1.50\,(+0.35, 0.29)$	(*81*)
CM2	2250	$148\,(+77, -51)$	$0.0619\,(+0.0323, -0.0212)$	(*81*)
CO3	3030	$1530\,(+1710, -810)$	$0.643\,(+0.718, -0.339)$	(*81*)
CR2	3100	$1630\,(+570, -420)$	$0.681\,(+0.238, -0.176)$	(*81*)
CV3	2950	178	0.0745	(*81*)
CV3o	2790	$452\,(+2709, -388)$	$0.190\,(+1.135, -0.162)$	(*81*)
CV3r	3115	$284\,(+1370, -920)$	$1.19\,(+0.57, -0.39)$	(*81*)
EH	3720	$1330\,(+510, -370)$	$0.557\,(+0.213, 0.154)$	(*81*)
EL	3550	$394\,(+299, -170)$	$0.165\,(+0.125, -0.071)$	(*81*)
R	3030$^{\sharp}$	$138\,(+281, -92)$	$0.0577\,(+0.1179, -0.0387)$	(*81*)
Achondrites				
Angrites	3200	$29.7\,(+105.2, -23.1)$	$0.0124\,(+0.0441, -0.0097)$	(*82*)
Aubrites	3120	$7.48\,(+9.48, -4.18)$	$0.00314\,(+0.00397, -0.00175)$	(*82*)
Brachinites	3300	250	0.105	(*82*)
Diogenites	3230	$5.04\,(+5.00, -2.51)$	$0.00211\,(+0.00210, -0.00105)$	(*82*)
Eucrites	2900	$1.57\,(+2.31, -0.94)$	$0.000659\,(+0.000968, -0.000392)$	(*82*)
Howardites	2970	$10.8\,(+9.7, -5.1)$	$0.00452\,(+0.00405, -0.00213)$	(*82*)
Mesosiderites	4250	$985\,(+3349, -761)$	$0.413\,(+1.403, -0.319)$	(*82*)
Ureilites	3050	$1920\,(+2110, -1010)$	$0.806\,(+0.883, -0.421)$	(*82*)

* Densities from (*83–85*).

† Multisample averages and ± 1-σ variability in parentheses calculated assuming a log-normal distribution.

$^{\sharp}$ Using a density equal to that of CO chondrites.

Table S4. Summary of impact simulations.

Figure number	Impactor diameter, km	Impact velocity, km s^{-1}	Impact angle, degrees	Crust resolution, km	Percent projectile retained[†]		EOS table version[♯]
					mantle	core	
Differentiated impactors							
S1, top	200	15	45	10	(⋆)	90	2
S1, middle	200	15	45	20	4	83	2
S1, bottom	200	15	45	40	4	94	2
S2A	150	30	30	20	0	0.06	2
S2B	150	30	45	20	0.02	0.2	2
—	150	30	60	20	0	0	2
S3A	200	15	30	20	2	100	2
3, S3B	200	15	45	20	0.5	79	2
S3C	200	15	60	20	0	0.7	2
S4A	260	10	30	40	51	100	2
S4B	260	10	45	20	56	71	2
S4C	260	10	60	20	3	18	2
Homogeneous impactors							
S5, top	250	15	45	10	16	—	1
S5, middle	250	15	45	20	11	—	2
S5, bottom	250	15	45	40	13	—	2
S6A	158	30	30	40	3	—	1
S6B	158	30	45	40	0.4	—	1
—	158	30	45	40	0	—	1
S7A	250	15	30	40	79	—	1
S7B	250	15	45	10	16	—	1
S7C	250	15	60	40	1	—	1
S8A	300	10	30	20	74	—	2
S8B	300	10	45	40	36	—	2
S8C	300	10	60	20	5	—	2

[†] Not including retained widely dispersed vaporized materials, which would finely coat the lunar surface.

[♯] The calculations used SESAME-style equations of state (*86*), where pressure and energy are tabulated over a density-temperature grid. Version 2 of the forsterite and silica tables had a finer grid spacing in the vapor region of the phase diagram than version 1.

[⋆] Not calculated.

References

1. P. Dyal, C. W. Parkin, W. D. Daily, *Rev. Geophys. Space Phys.* **12**, 568 (1974).

2. L. Hood, *et al.*, *J. Geophys. Res.* **106**, 27,825 (2001).

3. D. L. Mitchell, *et al.*, *Icarus* **194**, 401 (2008).

4. M. E. Purucker, J. B. Nicholas, *J. Geophys. Res.* **115**, E12007 (2010).

5. M. Fuller, S. M. Cisowski, *Geomagnetism*, J. A. Jacobs, ed. (Academic Press, London, 1987), vol. 2, pp. 307–455.

6. J. Gattacceca, *et al.*, *Earth Planet. Sci. Lett.* **299**, 42 (2010).

7. W. D. Daily, P. Dyal, *Phys. Earth Planet. Int.* **20**, 255 (1979).

8. L. L. Hood, Z. Huang, *J. Geophys. Res.* **96**, 9837 (1991).

9. D. Crawford, P. Schultz, *Int. J. Impact Eng.* **23**, 169 (1999).

10. D. R. Stegman, A. M. Jellinek, S. A. Zatman, J. R. Baumgardner, M. A. Richards, *Nature* **421**, 143 (2003).

11. M. A. Wieczorek, *et al.*, *New views of the Moon*, B. J. Jolliff, M. A. Wieczorek, C. K. Shearer, C. R. Neal, eds. (Mineral. Soc. Amer., 2006), vol. 60 of *Rev. Min. Geochem.*, pp. 221–364.

12. M. Le Bars, M. Wieczorek, . Karatekin, D. Cbron, M. Laneuville, *Nature* **479**, 215 (2011).

13. C. Dwyer, D. Stevenson, F. Nimmo, *Nature* **479**, 212 (2011).

14. L. Hood, *Icarus* **211**, 1109 (2011).

15. J. Halekas, R. Lin, D. Mitchell, *Meteorit. Planet. Sci.* **38**, 565 (2003).

16. J. Halekas, *et al*., *J. Geophys. Res.* **106**, 27,841 (2001).

17. L. Hood, N. Artemieva, *Icarus* **193**, 485 (2008).

18. D. Wang, R. Van der Voo, D. R. Peacor, *Geosphere* **1**, 138 (2005).

19. P. Rochette, J. Gattacceca, A. V. Ivanov, M. A. Nazarov, N. S. Bezaeva, *Earth Planet. Sci. Lett.* **292**, 383 (2010).

20. I. Garrick-Bethell, B. P. Weiss, D. L. Shuster, J. Buz, *Science* **323**, 356 (2009).

21. E. K. Shea, *et al*., *Science* **335**, 453 (2012).

22. R. L. Korotev, *J. Geophys. Res.* **105**, 4317 (2000).

23. I. Garrick-Bethell, M. T. Zuber, *Icarus* **204**, 399 (2009).

24. R. Tagle, L. Hecht, *Meteorit. Planet. Sci.* **41**, 1721 (2006).

25. R. Tagle, R. T. Schmitt, J. Erzinger, *Geochim. Cosmochim. Acta* **73**, 4891 (2009).

26. R. L. Korotev, *J. Geophys. Res.* **92**, E491 (1987).

27. E. Pierazzo, H. J. Melosh, *Meteorit. Planet. Sci.* **35**, 117 (2000).

28. L. E. Senft, S. Stewart, *Earth Planet. Sci. Lett.* **287**, 471 (2009).

29. A. Brecher, L. Albright, *J. Geomag. and Geoelectr.* **29**, 379 (1977).

30. J. C. Andrews-Hanna, M. T. Zuber, W. B. Banerdt, *Nature* **453**, 1212 (2008).

31. M. M. Marinova, O. Aharonson, E. Asphaug, *Nature* **453**, 1216 (2008).

32. J. E. P. Connerney, *et al*., *Geophys. Res. Lett.* **28**, 4015 (2001).

33. D. J. Dunlop, J. Arkani-Hamed, *J. Geophys. Res.* **110**, E12S04 (2005).

34. D. E. Smith, *et al*., *Geophys. Res. Lett.* **37**, L18204 (2010).

35. D. J. Dunlop, K. S. Argyle, *J. Geophys. Res.* **102**, 20199 (1997).

36. P. A. Selkin, J. S. Gee, L. Tauxe, *Earth Planet. Sci. Lett.* **256**, 81 (2007).

37. R. Shaar, *et al*., *Earth Planet. Sci. Lett.* **290**, 201 (2010).

38. S. K. Runcorn, *Phys. Earth Planet. Inter.* **10**, 327 (1975).

39. G. Kletetschka, M. H. Acuna, T. Kohout, P. J. Wasilewski, J. E. P. Connerney, *Earth Planet. Sci. Lett.* **226**, 521 (2004).

40. J. Gattacceca, P. Rochette, *Earth Planet. Sci. Lett.* **227**, 377 (2004).

41. Y. Yu, *Geochem. Geophys. Geosyst.* **11**, Q02Z12 (2010).

42. T. Kobayashi, J. H. Kim, S. R. Lee, H. Araki, T. Ono, *IEEE Geosci. Remote Sensing Lett.* **7**, 435 (2010).

43. O. Aharonson, M. T. Zuber, S. C. Solomon, *Earth Planet. Sci. Lett.* **218**, 261 (2004).

44. D. A. Varshalovich, A. N. Moskalev, V. K. Khersonskii, *Quantum theory of angular momentum* (World Scientific, Singapore, 1988).

45. J. McGlaun, S. Thompson, M. Elrick, *Int. J. Impact Eng.* **10**, 351 (1990).

46. D. A. Crawford, *Proceedings of the 11th Hypervelocity Impact Symposium*, F. Schafer, S. Hiermaier, eds. (Fraunhofer Verlag, 2011), pp. 693–704.

47. T. Spohn, W. Konrad, D. Breuer, R. Ziethe, *Icarus* **149**, 54 (2001).

48. G. I. Kerley, *Sandia National Laboratory Tech. Rep.* **SAND93-0027** (1993).

49. W. Benz, A. G. W. Cameron, H. J. Melosh, *Icarus* **81**, 113 (1989).

50. H. J. Melosh, *Meteorit. Planet. Sci.* **42**, 2079 (2007).

51. J. R. Rice, *J. Geophys. Res.* **111**, B05311 (2006).

52. R. V. Zucker, S. T. Stewart, *Lunar Planet. Sci. Conf.* **41**, Abstract 2460 (2010).

53. T. Kawazoe, S.-i. Karato, K. Otsuka, Z. Jing, M. Mookherjee, *Phys. Earth Planet. Int.* **174**, 128 (2009).

54. J. Zhang, C. Herzberg, *J. Geophys. Res.* **99**, 17729 (1994).

55. B. A. Ivanov, H. J. Melosh, E. Pierazzo, *Large Meteorite Impacts and Planetary Evolution IV*, R. L. Gibson, W. U. Reimold, eds. (Geol. Soc. Amer., Boulder, CO, 2010), pp. 29–49.

56. S. K. Croft, *J. Geophys. Res.* **88**, B71 (1983).

57. R. M. Iverson, *Rev. Geophys.* **35**, 245 (1997).

58. P. Del Gaudio, *et al.*, *J. Geophys. Res.* **114**, B06306 (2009).

59. D. L. Kohlstedt, *Rev. Mineral. Geochem.* **51**, 121 (2002).

60. I. Garrick-Bethell, F. Nimmo, M. A. Wieczorek, *Science* **330**, 949 (2010).

61. D. A. Morrison, *Lunar Planet. Sci.* **29**, abstract 1657 (1998).

62. M. Le Feuvre, M. A. Wieczorek, *Icarus* **214**, 1 (2011).

63. E. Pierazzo, A. M. Vickery, H. J. Melosh, *Icarus* **127**, 408 (1997).

64. M. A. Wieczorek, M. T. Zuber, *J. Geophys. Res.* **106**, 27,825 (2001).

65. S. M. Cisowski, D. W. Collinson, S. K. Runcorn, A. Stephenson, M. Fuller, *J. Geophys. Res.* **88**, A691 (1983).

66. D. W. Collinson, S. K. Runcorn, A. Stephenson, A. J. Manson, *Proc. Lunar Planet. Sci. Conf.* **3**, 2343 (1972).

67. T. Nagata, R. M. Fisher, F. C. Schwerer, M. D. Fuller, J. R. Dunn, *Proc. Lunar Planet. Sci. Conf.* **2**, 2461 (1971).

68. T. Nagata, R. M. Fisher, F. C. Schwerer, *Moon* **4**, 160 (1972).

69. R. B. Hargraves, N. Dorety, *Proc. Lunar Planet. Sci. Conf.* **2**, 2477 (1971).

70. M. Fuller, E. Meshkov, S. M. Cisowski, C. J. Hale, *Proc. Lunar Planet. Sci. Conf.* **10**, 2211 (1979).

71. J. R. Dunn, M. Fuller, *Moon* **4**, 49 (1972).

72. G. W. Pearce, W. A. Gose, D. W. Strangway, *Proc. Lunar Planet. Sci. Conf.* **4**, 3045 (1973).

73. T. Nagata, R. M. Fisher, F. C. Schwerer, M. D. Fuller, J. R. Dunn, *Proc. Lunar Planet. Sci. Conf.* **4**, 3019 (1973).

74. A. Brecher, W. H. Menke, K. R. Morash, *Proc. Lunar Planet. Sci. Conf.* **5**, 2795 (1974).

75. T. Nagata, *et al.*, *Proc. Lunar Planet. Sci. Conf.* **5**, 2827 (1974).

76. G. W. Pearce, D. W. Strangway, W. A. Gose, *Proc. Lunar Planet. Sci. Conf.* **5**, 2815 (1974).

77. I. Garrick-Bethell, B. P. Weiss, *Lunar Planet. Sci.* **38**, abstract 2405 (2007).

78. A. Brecher, D. J. Vaughan, R. G. Burns, K. R. Morash, *Proc. Lunar Planet. Sci. Conf.* **4**, 2991 (1973).

79. N. Sugiura, D. W. Strangway, *Proc. Lunar Planet. Sci. Conf.* **13**, A684 (1983).

80. P. Rochette, *et al.*, *Meteorit. Planet. Sci.* **38**, 251 (2003).

81. P. Rochette, *et al.*, *Meteorit. Planet. Sci.* **43**, 959 (2008).

82. P. Rochette, *et al*., *Meteorit. Planet. Sci.* **44**, 405 (2009).

83. D. T. Britt, G. J. Consolmagno, *Meteorit. Planet. Sci.* **38**, 1161 (2003).

84. G. Consolmagno, D. Britt, R. Macke, *Chemie der Erde / Geochemistry* **68**, 1 (2008).

85. D. T. Britt, R. J. Macke, W. Kiefer, G. J. Consolmagno, *Lunar Planet. Sci.* **41**, 1869 (2010).

86. K. Holian, *T-4 handbook of material properties data bases, vol. 1c: Equations of state*., Report LA-10160-MS (Los Alamos National Laboratory, Los Alamos, NM, 1984).